J. Fluid Mech. (2007), *vol.* 576, *pp.* 1–25.
doi:10.1017/S0022112006004228 Printed in the United Kingdom

Stability of helical tip vortices in a rotor far wake

V. L. OKULOV[1,2] AND J. N. SØRENSEN[1]

[1] Department of Mechanical Engineering, Technical University of Denmark, Nils Koppels Allé, 403, DK-2800 Kongens Lyngby, Denmark

[2] Institute of Thermophysics, SB RAS, Lavrentyev Ave. 1, Novosibirsk, 630090, Russia

(Received 4 November 2005 and in revised form 19 September 2006)

As a means of analysing the stability of the wake behind a multi-bladed rotor the stability of a multiplicity of helical vortices embedded in an assigned flow field is addressed. In the model the tip vortices in the far wake are approximated by infinitely long helical vortices with constant pitch and radius. The work is a further development of a model developed in Okulov (*J. Fluid Mech.*, vol. 521, p. 319) in which the linear stability of N equally azimuthally spaced helical vortices was considered. In the present work the analysis is extended to include an assigned vorticity field due to root vortices and the hub of the rotor. Thus the tip vortices are assumed to be embedded in an axisymmetric helical vortex field formed from the circulation of the inner part of the rotor blades and the hub. As examples of inner vortex fields we consider three generic axial columnar helical vortices, corresponding to Rankine, Gaussian and Scully vortices, at radial extents ranging from the core radius of a tip vortex to several rotor radii.

The analysis shows that the stability of tip vortices largely depends on the radial extent of the hub vorticity as well as on the type of vorticity distribution. As part of the analysis it is shown that a model in which the vortex system is replaced by N tip vortices of strength Γ and a root vortex of strength $-N\Gamma$ is unconditionally unstable.

1. Introduction

The flow behind rotor systems, such as propellers, wind turbines, screws, or helicopter rotors, is dominated by a system of strong trailing tip vortices that governs the dynamics of the wake. The wake can generally be divided into two distinct parts, near wake and far wake. Near-wake features are related to the genesis of the vortex system where the presence of the rotor is felt directly. The far wake is usually the downstream position where the wake dynamics does not depend on rotor characteristics. In the present analysis we consider only the far wake and assume it to be in a state where it extends infinitely upstream and infinitely downstream with the same properties. This enables a stability analysis to be carried out locally in a plane perpendicular to the rotor axis, the so-called Trefftz plane, and attention is mainly focused on instability properties of a multiplicity of helical tip vortices. Such an analysis has practical applications mainly in helicopter and wind turbine aerodynamics. The geometry of the wake beneath a helicopter rotor is important for predicting accurately air loads on the blades in hover or vertical flight. The instability of the wake geometry is felt directly by the rotor and may have an impact on performance, vibrations, acoustics, etc. Modern wind turbines are often grouped in wind parks or 'wind farms'. At some wind conditions some turbines may be in the

wakes of others. This increases the fatigue loads and hence reduces the lifetime of the turbine. In some cases the vortices become unstable and break down. It is clear that if a wind turbine is located in a wake consisting of stable tip vortices, the fatigue loading is more severe than if the vortices have broken down by instability.

As basic hypothesis for the far-wake modelling we assume that the wake is fully developed and that the vorticity is concentrated in Nhelical tip vortices and a hub or root vortex lying along the system axis. This $(N+1)$-vortex system consisting of an array of infinitely long helical vortex lines with constant pitch and radius can be considered as an extension of the wake description proposed by Joukowski in 1912 for a two-bladed propeller (see also Margoulis 1922). To distinguish between propeller and turbine states the circulation of the tip vortices is taken as positive when power is added to the flow and negative when power is subtracted from the flow. Another difference is that the wake is expanding for a turbine whereas it is contracting for a propeller. The stability problem, however, is similar for both types of rotor systems.

Gupta & Loewy (1974) were the first to consider the stability of a multiplicity of helical vortices as a means of modelling tip vortices in rotor far wakes. Their analysis dealt with the stability of centreline perturbations of the helical vortex system. They extended the results of Levy & Forsdyke (1928) and Widnall (1972), who analysed the linear stability of a multiplicity of single twisted helices using the so-called cutoff approximation. Later numerical investigations of tip vortex stability beneath a helicopter rotor are due to Bhagwat & Leishman (2000). In both investigations the helical multiple was found to be unstable. This result is, however, in contradiction to visualizations of rotor wakes showing that helical tip vortices subject small pitch values are stable (see e.g. Vermeer, Sorensen & Crespo 2003). A limitation of the above cited works is that the far wake is treated as consisting of helical vortices generated by the blade tips only. This strongly restricts the possible variety of far-wake structures arising behind multi-bladed rotors operating at different modes. To cover stability for all possible operating regimes it is necessary to consider tip vortices embedded in a wake flow generated by the trailing vortex sheet of the blades and the root vortex as well.

In this context, the purpose of the present work is to define how different types of assigned or prescribed flows influence the stability of multiple helical tip vortices.

2. Theory: stability analysis

In this section the theory of linear stability of a multiplicity of helical vortices in equilibrium is treated. The analysis is a generalization of the model by Okulov (2004) in order to cover more complex flow problems in which the helical vortices are embedded in a vorticity-dominated assigned inviscid flow field.

The influence of an assigned flow on the stability of multiple vortices has so far only been studied for a circular array of point vortices or straight vortex filaments (the limiting case of a helical vortex with infinite pitch). In 1931 Havelock determined the influence of an assigned flow on the stability properties. He found that if the assigned flow is rotating like a rigid body the conditions for stability are the same as for helical vortices in free space. On the other hand, if the assigned flow is induced by a central point vortex with a total circulation that equals the negative sum of the circulation of the vortex array, then the system is unconditionally unstable. Later, Morikawa & Swenson (1971) found stable limits for the central vortex circulation. Up to now, however, nobody has studied the influence of an assigned flow on helical vortex stability.

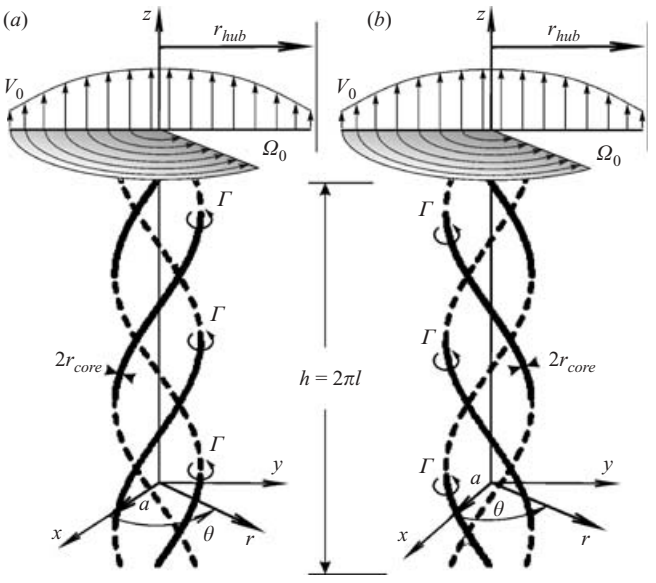

FIGURE 1. Sketch and notation for a circular equilibrium array of right-handed (*a*) and left-handed (*b*) helical vortices in an assigned flow field with angular velocity Ω_0 and axial velocity V_0.

As a basic configuration we consider the linear stability of infinitesimal spatial displacements of an equilibrium helical vortex configuration $\Lambda^{\pm}$ (see figure 1). The vortex system $\Lambda^{\pm}$ consists of N identical slender right- or left-handed helical vortices of circulation Γ and constant pitch h, or $l = h/2\pi$, with their vortex axes lying on a cylinder with radius a and displaced azimuthally by an angle $\phi = 2\pi/N$. In the following we use a double sign notation in which the upper sign refers to right-handed helical vortices and the lower sign to left-handed ones. Dimensionless pitch is introduced as $\tau = l/a$. The vortex cores are assumed circular with radius r_{core}, or, in dimensionless form, $\sigma = r_{core}/a$, where $\sigma \ll 1$. The vortex system is subject to the additional constraints that $2\sigma < \tau$ and $N < \pi/\sigma$. The vortex cores are superposed with helical vortex filaments which are co-linear to the lines that define the centre of the vortex:

$$r = a, \quad z \mp l(\theta + n\phi) = \chi_0 \equiv \text{const.} \tag{2.1}$$

The vorticity of the vortex cores is uniformly distributed across the core cross-sections (see e.g. Ricca 1994).

The assigned flow is assumed to be subject to the same helical symmetry as the basic helical vortex configuration $\Lambda^{\pm}$. This means that the following relation exists between the components of the vorticity vector (Okulov 2004):

$$\omega_r = 0; \quad \omega_\theta/\omega_z = \pm r/l \quad \text{or} \quad \omega_\theta \mp \frac{r}{l}\omega_z = 0. \tag{2.2}$$

Assuming inviscid flow conditions, the vorticity components satisfy the transport equations of Euler, which in helical variables (r, $\chi = \theta \mp z/l$) reduce to the following set of equations:

$$\frac{\partial \omega_r}{\partial t} + u_r \frac{\partial \omega_r}{\partial r} + \left(u_\theta \mp \frac{r}{l}u_z\right)\frac{\partial \omega_r}{r\,\partial \chi} = \omega_r \frac{\partial u_r}{\partial r} + \left(\omega_\theta \mp \frac{r}{l}\omega_z\right)\frac{\partial u_r}{r\,\partial \chi}, \tag{2.3a}$$

$$\frac{\partial \omega_\theta}{\partial t} + u_r \frac{\partial \omega_\theta}{\partial r} + \left(u_\theta \mp \frac{r}{l} u_z\right) \frac{\partial \omega_\theta}{r\,\partial \chi} - \frac{u_r \omega_\theta}{r} = \omega_r \frac{\partial u_\theta}{\partial r} + \left(\omega_\theta \mp \frac{r}{l} \omega_z\right) \frac{\partial u_\theta}{r\,\partial \chi} - \frac{u_\theta \omega_r}{r}, \tag{2.3b}$$

$$\frac{\partial \omega_z}{\partial t} + u_r \frac{\partial \omega_z}{\partial r} + \left(u_\theta \mp \frac{r}{l} u_z\right) \frac{\partial \omega_z}{r\,\partial \chi} = \omega_r \frac{\partial u_z}{\partial r} + \left(\omega_\theta \mp \frac{r}{l} \omega_z\right) \frac{\partial u_z}{r\,\partial \chi}. \tag{2.3c}$$

From (2.2) it is readily seen that the right-hand sides of the equations are equal to zero, implying that the vorticity does not vary along a trajectory of fluid particles.

As a further simplification, the assigned velocity field is assumed to consist of a rotating flow with angular velocity $\Omega_0(r)$ around the oz-axis of the vortex system $\Lambda^\pm$ and a translating velocity $V_0(r)$ along the oz-axis. Such a non-perturbed $\Lambda^\pm$ vortex system rotates with angular velocity

$$\Omega(a) = \Omega_0(a) + \Omega_{Ind} + \Omega_{Sind},$$

and moves uniformly along the axis of a cylinder of radius $a$with axial velocity

$$V(a) = V_0(a) + V_{Ind} + V_{Sind},$$

where subscript 'Ind' refers to induction and '$Sind$' to self-induction. The total velocity components are divided into three parts: (i) an invariant assigned flow field; (ii) an induced flow field due to induction from the helical vortices on the surroundings; (iii) a flow field due to self-induction, i.e. the velocity induced by an individual helical vortex on its own trajectory. Note that in contrast to the plane case (Havelock 1931), where the total vortex motion consists of an assigned flow field and the mutual induction of the vortices, we also include self-induction.

Let the kth vortex ($k \in [0, N-1]$) from $\Lambda^\pm$ be simultaneously displaced from the equilibrium position $r = a$ and $\theta = 2\pi k/N$ in a moving plane $(r, \theta + \Omega t, z + Vt)$ fixed at $z = \text{const}$, such that $(r, \theta, z) = (a + r_k, 2\pi k/N + \Omega t + \theta_k, z + Vt + z_k)$; then the equations of motion of the kth disturbed vortex in the plane $z = 0$, for example, can be written as

$$\frac{\mathrm{d}}{\mathrm{d}t}(a + r_k) = \sum_{n(n \neq k)} u_r\left(a + r_k, a + r_n, \frac{2\pi(n-k)}{N} + \chi_k - \chi_n\right), \tag{2.4a}$$

$$\begin{aligned}(a + r_k)\frac{\mathrm{d}}{\mathrm{d}t}\left(\frac{2\pi k}{N} + t[\Omega_{Ind} + \Omega_{Sind} + \Omega_0] + \theta_k\right) \\ = (a + r_k)[\Omega_{Sind}(a + r_k) + \Omega_0(a + r_k)] \\ + \sum_{n(n \neq k)} u_\theta\left(a + r_k, a + r_n, \frac{2\pi(n-k)}{N} + \chi_k - \chi_n\right),\end{aligned} \tag{2.4b}$$

$$\begin{aligned}&\frac{\mathrm{d}}{\mathrm{d}t}(t[V_{Ind} + V_{Sind} + V_0] + z_k) \\ &\quad = V_{Sind}(a + r_k) + V_0(a + r_k) + \sum_{n(n \neq k)} u_z\left(a + r_k, a + r_n, \frac{2\pi(n-k)}{N} + \chi_k - \chi_n\right).\end{aligned} \tag{2.4c}$$

The velocity field $\boldsymbol{u} = (u_r, u_\theta, u_z)$ induced by a single helical vortex is defined in helical variables $(r, \chi = \theta \mp z/l)$, i.e. $\boldsymbol{u} = \boldsymbol{u}(r, a, \chi - \chi_0)$ is the value of the velocity at point (r, χ) induced by the helical vortices with axes at points (a, χ_0). Introducing the displacement of the i-vortex core from (2.1) in helical variables as

$$r_i \quad \text{and} \quad \chi_i = \theta_i \mp z_i/l, \tag{2.5}$$

the disturbed positions of the fixed n-vortex and calculated reference k-point in system (2.4) are given as $(a+r_n, 2\pi n/N+\chi_n)$ and $(a+r_k, 2\pi k/N+\chi_k)$ respectively. The velocity of points situated outside the vortex cores $\Lambda^{\pm}$ may be determined by use of Hardin's (1982) solution here extended to both types of helical symmetry (figure 1):

$$u_r(r,a,\chi-\chi_0)=\frac{\Gamma a}{\pi l^2}\mathrm{Im}\left\{\begin{matrix}H_1^{1,1}(r/l,a/l,\chi-\chi_0)\\H_1^{1,1}(a/l,r/l,\chi-\chi_0)\end{matrix}\right\}, \tag{2.6a}$$

$$u_\theta(r,a,\chi-\chi_0)=\frac{\Gamma}{2\pi r}\left\{\begin{matrix}0\\1\end{matrix}\right\}+\frac{\Gamma a}{\pi r l}\mathrm{Re}\left\{\begin{matrix}H_1^{0,1}(r/l,a/l,\chi-\chi_0)\\H_1^{1,0}(a/l,r/l,\chi-\chi_0)\end{matrix}\right\}, \tag{2.6b}$$

$$u_z(r,a,\chi-\chi_0)=\pm\frac{\Gamma}{2\pi l}\left\{\begin{matrix}1\\0\end{matrix}\right\}\mp\frac{\Gamma a}{\pi l^2}\mathrm{Re}\left\{\begin{matrix}H_1^{0,1}(r/l,a/l,\chi-\chi_0)\\H_1^{1,0}(a/l,r/l,\chi-\chi_0)\end{matrix}\right\}, \tag{2.6c}$$

where the terms in the braces are defined such that the upper one corresponds to $r<a$ and the lower one to $r>a$. Rewriting the Kapteyn series $H_M^{I,J}(x,y,\chi)$ for $x\leqslant y$ with singularity isolation using the procedure of Okulov (2004), we obtain

$$H_M^{I,J}(x,y,\chi)=\sum_{m=1}^{\infty}m^M h_m^{I,J}(x,y)\mathrm{e}^{\mathrm{i}m\chi}\equiv C_{M,0}^{I,J}\frac{\mathrm{e}^{\xi+\mathrm{i}\chi}}{(\mathrm{e}^{\xi}-\mathrm{e}^{\mathrm{i}\chi})^2}+C_{M,1}^{I,J}\frac{\mathrm{e}^{\mathrm{i}\chi}}{\mathrm{e}^{\xi}-\mathrm{e}^{\mathrm{i}\chi}}$$
$$+C_{M,2}^{I,J}\ln(1-\mathrm{e}^{-\xi+\mathrm{i}\chi})+C_{M,3}^{I,J}\mathrm{Li}_2(\mathrm{e}^{-\xi+\mathrm{i}\chi})+C_{M,4}^{I,J}\mathrm{Li}_3(\mathrm{e}^{-\xi+\mathrm{i}\chi})+\sum_{m=1}^{\infty}m^M ri_m^{I,J}(x,y)\mathrm{e}^{\mathrm{i}m\chi}, \tag{2.7}$$

where $h_m^{I,J}(x,y)=I_m^{\langle I\rangle}(mx)K_m^{\langle J\rangle}(my)$ is the product of modified Bessel functions if I or $J=0$ and their derivatives if I or $J=1$; Li_2 and Li_3 are polylogarithms;

$$\mathrm{e}^{\xi}=\frac{x}{y}\frac{\exp\sqrt{1+x^2}}{1+\sqrt{1+x^2}}\frac{1+\sqrt{1+y^2}}{\exp\sqrt{1+y^2}};$$

$$C^{I,J}=\frac{2x^{-I}}{(-y)^J}\frac{(\sqrt{1+x^2})^{I-1/2}}{(\sqrt{1+y^2})^{1/2-J}}\begin{bmatrix}0&0&1&\alpha^{I,J}&\beta^{I,J}\\0&1&\alpha^{I,J}&\beta^{I,J}&\gamma^{I,J}\\1&\alpha^{I,J}&\beta^{I,J}&\gamma^{I,J}&0\end{bmatrix};$$

$$ri_m^{I,J}(x,y)=I_m^{\langle I\rangle}(mx)K_m^{\langle J\rangle}(my)-(\mathrm{e}^{\chi})^m\frac{2x^{-I}}{(-y)^J}\frac{(\sqrt{1+x^2})^{I-1/2}}{(\sqrt{1+y^2})^{1/2-J}}\left(1+\frac{\alpha^{I,J}}{m}+\frac{\beta^{I,J}}{m^2}+\frac{\gamma^{I,J}}{m^3}\right)$$

and the coefficients in $\alpha^{I,J}$, $\beta^{I,J}$, $\gamma^{I,J}$ are obtained as a result of multiplication of the uniform expansion of cylindrical Bessel functions (see Appendix C in Fukumoto & Okulov 2005). We will use the second form of the Kapteyn series with singularity isolation because the coefficients $h_m^{I,J}$ of the initial trigonometric series grow indefinitely with m in the neighbourhood of $x=y(=1)$ in the first form, invalidating all calculations of the series there. In contrast, as proved by Okulov & Fukumoto (2004), in the second form the decrease in magnitude of the coefficients $ri_m^{I,J}$ with m is rapid in the whole range of x. In the event that a high accuracy is required the form with singularity isolation should be considered.

The velocity field induced by right- and left-hand helical vortex filaments differs in the sign of the axial velocity component and in the definition of the helical variable $\chi=\theta\mp z/l$. Using a triad of tangent, normal and binormal unit vectors along a helical

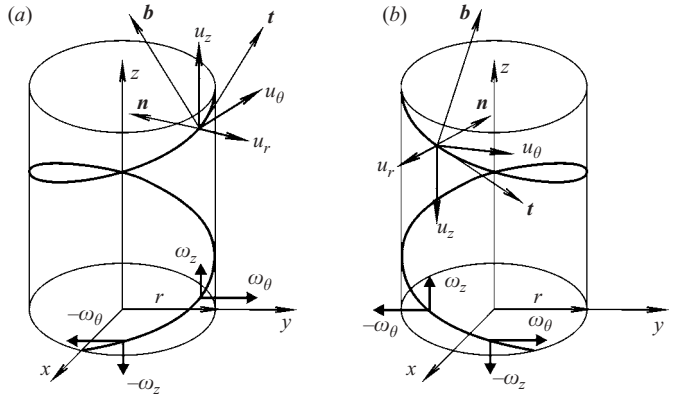

FIGURE 2. Triad of unit vectors for vortex axis with right (*a*) and left (*b*) helical symmetry and vorticity components for helix circulation with different sign.

vortex line (figure 2), we obtain

$$\boldsymbol{t}^{\pm} = \left(0, \pm\frac{r}{\sqrt{r^2+l^2}}, \frac{l}{\sqrt{r^2+l^2}}\right), \quad \boldsymbol{n}^{\pm} = (-1, 0, 0), \quad \boldsymbol{b}^{\pm} = \left(0, \mp\frac{l}{\sqrt{r^2+l^2}}, \frac{r}{\sqrt{r^2+l^2}}\right).$$

The corresponding velocity components are given as

$$u_\tau^{\pm} = \pm\frac{\sqrt{r^2+l^2}}{l}\boldsymbol{t}\cdot\boldsymbol{u} = u_z \pm \frac{r}{l}u_\theta \equiv \pm\text{const}, \quad u_n^{\pm} = -u_r,$$
$$u_\chi^{\pm} = \mp\frac{\sqrt{r^2+l^2}}{l}\boldsymbol{b}\cdot\boldsymbol{u} = u_\theta \mp \frac{r}{l}u_z. \tag{2.8}$$

It has been shown by Okulov (2004) that vorticity fields with helical symmetry attain a constant value of $u_\tau^{\pm}$ at all points in the flow field, including the cores of the helical vortices $\Lambda^{\pm}$. When inserting (2.6*b*) and (2.6*c*) into (2.8) for flows induced by either a vortex system of type Λ^+ or of type Λ^-, i.e. with right- or left-handed helical symmetry, it is easily seen that the value of $u_\chi^{\pm}$ is the same, whereas $u_\tau^{\pm}$ depends on the sign. For simplicity, $u_\chi^{\pm}$ will in the following be referred to as u_χ, and the assigned flow will be denoted u_{0_χ}. Combining (2.4*b*) and (2.4*c*) with (2.5) and (2.8) results in the following equation:

$$(a+r_k)\frac{\mathrm{d}}{\mathrm{d}t}\left(\frac{2\pi k}{N} + \frac{t}{a}\left[u_{Ind_\chi} + u_{Sind_\chi} + u_{0_\chi}\right] + \chi_k\right)$$
$$= u_{Sind_\chi}(a+r_k) + u_{0_\chi}^{\pm}(a+r_k) + \sum_{n(n\neq k)} u_\chi\left(a+r_k, a+r_n, \frac{2\pi(n-k)}{N} + \chi_k - \chi_n\right), \tag{2.9}$$

hence reducing the system (2.4) to two equations (2.4*a*) and (2.9) in helical variables.

The velocity of the assigned flow field is given by

$$u_{0_\chi}(r) = r[\Omega_0(r) - V_0(r)/l]. \tag{2.10}$$

By linearizing r_k, r_n, χ_k, χ_n a linear approximation of (2.4*a*) and (2.9) for the motion of the kth vortex can be written as

$$\frac{\mathrm{d}r_k}{\mathrm{d}t} = \sum_{n(n\neq k)}\left[r_k\frac{\mathrm{d}}{\mathrm{d}r}u_r\left(a, a, \frac{2\pi(n-k)}{N}\right) + r_n\frac{\mathrm{d}}{\mathrm{d}a}u_r\left(a, a, \frac{2\pi(n-k)}{N}\right)\right]$$
$$+ \sum_{n(n\neq k)}\left[\chi_k\frac{\mathrm{d}}{\mathrm{d}\chi}u_r\left(a, a, \frac{2\pi(n-k)}{N}\right) + \chi_n\frac{\mathrm{d}}{\mathrm{d}\chi_0}u_r\left(a, a, \frac{2\pi(n-k)}{N}\right)\right], \tag{2.11a}$$

$$a\frac{\mathrm{d}\chi_k}{\mathrm{d}t} = -\frac{r_k}{a}\left[u_{Ind_\chi} + u_{Sind_\chi} + u_{0_\chi}\right] + r_k\frac{\mathrm{d}}{\mathrm{d}a}u_{Sind_\chi} + r_k\frac{\mathrm{d}}{\mathrm{d}r}u_{0_\chi}$$
$$+ \sum_{n(n\neq k)}\left[r_k\frac{\mathrm{d}}{\mathrm{d}r}u_\chi\left(a, a, \frac{2\pi(n-k)}{N}\right) + r_n\frac{\mathrm{d}}{\mathrm{d}a}u_\chi\left(a, a, \frac{2\pi(n-k)}{N}\right)\right]$$
$$+ \sum_{n(n\neq k)}\left[\chi_k\frac{\mathrm{d}}{\mathrm{d}\chi}u_\chi\left(a, a, \frac{2\pi(n-k)}{N}\right) + \chi_n\frac{\mathrm{d}}{\mathrm{d}\chi_0}u_\chi\left(a, a, \frac{2\pi(n-k)}{N}\right)\right]. \quad (2.11b)$$

Following Havelock (1931) we search for a solution of system (2.11*a*) and (2.11*b*) in the form

$$r_k = \alpha(t)\exp\left(2\pi\mathrm{i}\frac{ks}{N}\right), \quad \chi_k = \beta(t)\exp\left(2\pi\mathrm{i}\frac{ks}{N}\right).$$

Here s is the subharmonic wavenumber that takes values within the range $[1, N-1]$, corresponding to $N-1$ independent eigenfunctions. When $s=0$, the displacement of the vortices consists of a rotation combined with a small change in radius. The result is a new steady state with a corresponding small change in angular velocity.

When introducing the above perturbations the first sum in (2.11*a*) and the last sum in (2.11*b*) become identically zero (see Appendix A in Okulov 2004):

$$\alpha(t)\exp\left(2\pi\mathrm{i}\frac{ks}{N}\right)\frac{\Gamma}{\pi a^2}\sum_{m=1}^{\infty}\left[\left(\frac{1+\tau^2}{\tau^3}m^2h_m^{0,1}\left(\frac{1}{\tau}, \frac{1}{\tau}\right)\right.\right.$$
$$\left.\left.-\frac{1}{\tau}mh_m^{1,1}\left(\frac{1}{\tau}, \frac{1}{\tau}\right)\right)\sum_{n(n\neq k)}\sin\left(\frac{2\pi m(n-k)}{N}\right)\right]$$
$$+\alpha(t)\frac{\Gamma}{\pi a^2}\frac{1+\tau^2}{\tau^3}\sum_{m=1}^{\infty}\left[\left(m^2h_m^{0,1}\left(\frac{1}{\tau}, \frac{1}{\tau}\right)\right)\sum_{n(n\neq k)}\exp\left(2\pi\mathrm{i}\frac{ns}{N}\right)\sin\left(\frac{2\pi m(n-k)}{N}\right)\right] = 0,$$

$$-\beta(t)\exp\left(2\pi i\frac{ks}{N}\right)\frac{\Gamma}{\pi a}\frac{1+\tau^2}{\tau^3}\sum_{m=1}^{\infty}\left[m^2h_m^{0,1}\left(\frac{1}{\tau}, \frac{1}{\tau}\right)\sum_{n(n\neq k)}\sin\left(\frac{2\pi m(n-k)}{N}\right)\right]$$
$$+\beta(t)\frac{\Gamma}{\pi a}\frac{1+\tau^2}{\tau^3}\sum_{m=1}^{\infty}\left[m^2h_m^{0,1}\left(\frac{1}{\tau}, \frac{1}{\tau}\right)\sum_{n(n\neq k)}\exp\left(2\pi i\frac{ns}{N}\right)\sin\left(\frac{2\pi m(n-k)}{N}\right)\right] = 0.$$

Next, using sums of singularities situated on a circumference with identical displacement (see Appendix D in Okulov 2004) and Kapteyn series with singularity isolation, equation (2.7), the remainder sum in (2.11*a*), $\beta(t)\exp(2\pi\mathrm{i}ks/N)D_{Ind\,r}(N, s, \tau)$, and the remainder sum in (2.11*b*), $\alpha(t)\exp(2\pi\mathrm{i}ks/N)D_{Ind\,\chi}(N, s, \tau)$, may after some algebra be evaluated as

$$\frac{4\pi a}{\Gamma}D_{Ind\,r}(N, s, \tau) = s(N-s)\frac{\sqrt{1+\tau^2}}{\tau} - \frac{\tau}{4}\frac{4\tau^2-3}{(1+\tau^2)^{5/2}}\left(\frac{N}{s} - E - \psi\left(-\frac{s}{N}\right)\right)$$
$$+\frac{4}{\tau^2}\sum_{m=1}^{\infty}\left[m^2ri_m^{1,1}\left(\frac{1}{\tau}, \frac{1}{\tau}\right)\sum_{n=0}^{N-1}\left(1-\exp\left(2\pi\mathrm{i}\frac{ns}{N}\right)\right)\cos\left(2\pi\frac{nm}{N}\right)\right], \quad (2.12a)$$

$$\frac{4\pi a^2}{\Gamma}\frac{\tau^2}{1+\tau^2}D_{Ind\,\chi}(N,s,\tau)=s(N-s)\frac{\sqrt{1+\tau^2}}{\tau}-N+1+2\frac{N-2}{1+\tau^2}$$
$$+\frac{\tau^3}{(1+\tau^2)^{5/2}}\left(\ln(N)-\left(1-\frac{1}{4\tau^2}\right)\left(\frac{N}{s}-E-\psi\left(-\frac{s}{N}\right)\right)\right)$$
$$+\frac{\tau^3(1-\tau^2)}{(1+\tau^2)^{11/2}}\left(\tau^4-3\tau^2+\frac{3}{8}\right)\frac{N^2-1}{N^2}\varsigma(3)$$
$$+\frac{4}{\tau^2}\sum_{m=1}^{\infty}\left[\left(m^2\,ri_m^{1,1}\left(\frac{1}{\tau},\frac{1}{\tau}\right)+m\frac{\tau(1-\tau^2)}{(1+\tau^2)}ri_m^{0,1}\left(\frac{1}{\tau},\frac{1}{\tau}\right)\right)\sum_{n=0}^{N-1}\cos\left(2\pi\frac{nm}{N}\right)\right]$$
$$+\frac{4(1+\tau^2)}{\tau^2}\sum_{m=1}^{\infty}\left[m^2\,ri_m^{0,0}\left(\frac{1}{\tau},\frac{1}{\tau}\right)\sum_{n=0}^{N-1}\exp\left(2\pi\mathrm{i}\frac{ns}{N}\right)\cos\left(2\pi\frac{nm}{N}\right)\right],\qquad(2.12b)$$

where $E=0.577215\ldots$ is the Euler constant, and $\psi(\cdot)$ is the psi-function.

In accordance with the procedure described in Okulov (2004) an exact solution for the sum of the induced and the self-induced velocity components in (2.11*b*) may be derived as

$$\frac{4\pi a}{\Gamma}\left(u_{Ind\chi}+u_{Sind\chi}\right)=N-\frac{\sqrt{1+\tau^2}}{\tau}-\frac{N}{\tau^2}+\frac{1}{\tau(1+\tau^2)^{1/2}}\left(\ln\frac{N(1+\tau^2)^{3/2}}{\tau}-\ln\frac{1}{\sigma}+\frac{1}{4}\right)$$
$$-\frac{\tau}{(1+\tau^2)^{7/2}}\left(\tau^4-3\tau^2+\frac{3}{8}\right)\frac{\varsigma(3)}{N^2}+4\frac{1+\tau^2}{\tau^3}\sum_{m=1}^{\infty}\left[m\,ri_m^{1,0}\left(\frac{1}{\tau},\frac{1}{\tau}\right)\sum_{n=0}^{N-1}\cos\left(2\pi\frac{nm}{N}\right)\right]\qquad(2.13)$$

where the self-induced component is derived by setting $N=1$, i.e.

$$\frac{4\pi a}{\Gamma}u_{Sind\chi}=1-\frac{\sqrt{1+\tau^2}}{\tau}-\frac{1}{\tau^2}+\frac{1}{\tau(1+\tau^2)^{1/2}}\left(\ln\frac{(1+\tau^2)^{3/2}}{\tau}-\ln\frac{1}{\sigma}+\frac{1}{4}\right)$$
$$-\frac{\tau}{(1+\tau^2)^{7/2}}\left(\tau^4-3\tau^2+\frac{3}{8}\right)\varsigma(3)+4\frac{1+\tau^2}{\tau^3}\sum_{m=1}^{\infty}m\,ri_m^{1,0}\left(\frac{1}{\tau},\frac{1}{\tau}\right).\qquad(2.14)$$

The coefficients of the trigonometric series of the regular remainders are defined as

$$ri_m^{0,0}\left(\frac{1}{\tau},\frac{1}{\tau}\right)=I_m\left(\frac{m}{\tau}\right)K_m\left(\frac{m}{\tau}\right)-\frac{\tau}{2m(1+\tau^2)^{1/2}}\left(1-\frac{\tau^2}{2m^2(1+\tau^2)^3}\left(\tau^2-\frac{3}{4}\right)\right),$$

$$ri_m^{0,1}\left(\frac{1}{\tau},\frac{1}{\tau}\right)=I_m\left(\frac{m}{\tau}\right)K'_m\left(\frac{m}{\tau}\right)$$
$$+\frac{\tau}{2m}\left(1+\frac{\tau}{2m(1+\tau^2)^{3/2}}+\frac{\tau^3}{2m^3(1+\tau^2)^{9/2}}\left(\tau^4-3\tau^2+\frac{3}{8}\right)\right),$$

$$ri_m^{1,0}\left(\frac{1}{\tau},\frac{1}{\tau}\right)=I'_m\left(\frac{m}{\tau}\right)K_m\left(\frac{m}{\tau}\right)$$
$$-\frac{\tau}{2m}\left(1-\frac{\tau}{2m(1+\tau^2)^{3/2}}-\frac{\tau^3}{2m^3(1+\tau^2)^{9/2}}\left(\tau^4-3\tau^2+\frac{3}{8}\right)\right),$$

$$ri_m^{1,1}\left(\frac{1}{\tau},\frac{1}{\tau}\right)=I'_m\left(\frac{m}{\tau}\right)K'_m\left(\frac{m}{\tau}\right)+\frac{\tau(1+\tau^2)^{1/2}}{2m}\left(1+\frac{\tau^2}{2m^2(1+\tau^2)^3}\left(\tau^2-\frac{3}{4}\right)\right),$$

and

$$\sum_{n=0}^{N-1}\cos\left(2\pi\frac{nm}{N}\right)=\begin{cases}N & \text{if } m=kN\\ 0 & \text{if } m\neq kN\end{cases}\quad(k=1,2,3\ldots). \tag{2.15}$$

Now (2.12)–(2.14) are written as exact solutions, in contrast to the approximate formulae (4.8) and (4.10) in Okulov (2004) where only one term of the regular remainder ($m=1$) was maintained. Thus, the proposed formulae can be used with any desired precision. For example, a calculation of (2.14) with five terms of the regular remainder is in complete agreement with computations of Boersma & Wood (1999) and Wood & Boersma (2001) using six significant figures.

An additional term considered in (2.11*b*) is the derivative of the self-induced motion (2.14) that, after some algebra, takes the form

$$\begin{aligned}\frac{4\pi a^2}{\Gamma}\frac{\mathrm{d}}{\mathrm{d}a}u_{Sind_\chi}&=-1-\frac{1}{\tau^2}+\frac{\tau^4-\tau^2+1}{\tau(1+\tau^2)^{3/2}}+\frac{\tau}{(1+\tau^2)^{3/2}}\left(\ln\frac{(1+\tau^2)^{3/2}}{\tau}-\ln\frac{1}{\sigma}+\frac{1}{4}\right)\\&+\frac{\tau\,\varsigma(3)}{(1+\tau^2)^{9/2}}\left(\tau^6-4\tau^4+\frac{27}{8}\tau^2-\frac{3}{8}\right)+4\frac{1-\tau^2}{\tau^3}\sum_{m=1}^{\infty}\left[m\,ri_m^{1,0}\left(\frac{1}{\tau},\frac{1}{\tau}\right)\right]\\&+\frac{4(1+\tau^2)}{\tau^4}\sum_{m=1}^{\infty}\left[m^2\,ri_m^{1,1}\left(\frac{1}{\tau},\frac{1}{\tau}\right)+(1+\tau^2)\,m^2\,ri_m^{0,0}\left(\frac{1}{\tau},\frac{1}{\tau}\right)\right].\end{aligned} \tag{2.16}$$

In the previous work of Okulov (2004) the influence of a change in the self-induced movement of the vortices on the vortex stability, equation (2.16), was neglected. However, as will be shown below, the terms of (2.16) have a large influence on the stability properties.

From (2.11), the system of equations for α, β reduces to

$$\alpha'(t)=A(N,s,\tau)\beta,\quad \beta'(t)=B(N,s,\tau,\sigma,u_{0\chi})\alpha, \tag{2.17}$$

where

$$A=\frac{4\pi a}{\Gamma}D_{Ind\,r}\ \text{and}\ B=\frac{4\pi a^2}{\Gamma}\left[D_{Ind_\chi}+\frac{\mathrm{d}}{\mathrm{d}a}u_{Sind_\chi}-\frac{u_{Ind_\chi}+u_{Sind_\chi}}{a}\right]+\left(\frac{\mathrm{d}}{\mathrm{d}r}u_{0\chi}-\frac{u_{0\chi}}{a}\right).$$

This implies that α and β are proportional to $(t\sqrt{AB})$. Therefore, a system consisting of N helical vortices is unstable if $AB\geqslant 0$ for any combination of s, τ and ε.

Figure 3 shows a typical behaviour of A as a function of the vortex pitch τ for $s=1$ and various values of N. As A is positive for all values of s, τ and N, the stability condition only depends on the sign of B, which, for helical vortices in free space without an assigned flow, i.e. for $B(N,s,\tau,\sigma,0)\equiv B_0(N,s,\tau,\sigma)$, can be written in the form

$$\begin{aligned}B_0&=s(N-s)\frac{(1+\tau^2)^{3/2}}{\tau^3}-2N+2\frac{N-2}{\tau^2}+\frac{1+2\tau^2}{\tau(1+\tau^2)^{1/2}}\\&+\frac{1}{\tau(1+\tau^2)^{3/2}}\left[\left(\tau^2-\frac{1}{4}\right)\left(E+\psi\left(-\frac{s}{N}\right)-\frac{N}{s}\right)\right.\\&\left.+\frac{3}{4}-2\tau^2-\ln\left(N\varepsilon\frac{(1+\tau^2)^{3/2}}{\tau}\right)\right]+\frac{\tau^3}{(1+\tau^2)^{9/2}}\left(2\tau^4-6\tau^2+\frac{3}{4}\right)\frac{\varsigma(3)}{N^2}\\&+\frac{4(1+\tau^2)}{\tau^3}\sum_{m=1}^{\infty}\left[\left(\frac{m^2}{\tau}ri_m^{1,1}\left(\frac{1}{\tau},\frac{1}{\tau}\right)-m\,ri_m^{1,0}\left(\frac{1}{\tau},\frac{1}{\tau}\right)\right)\left(1+\sum_{n=0}^{N-1}\cos\left(2\pi\frac{nm}{N}\right)\right)\right]\end{aligned}$$

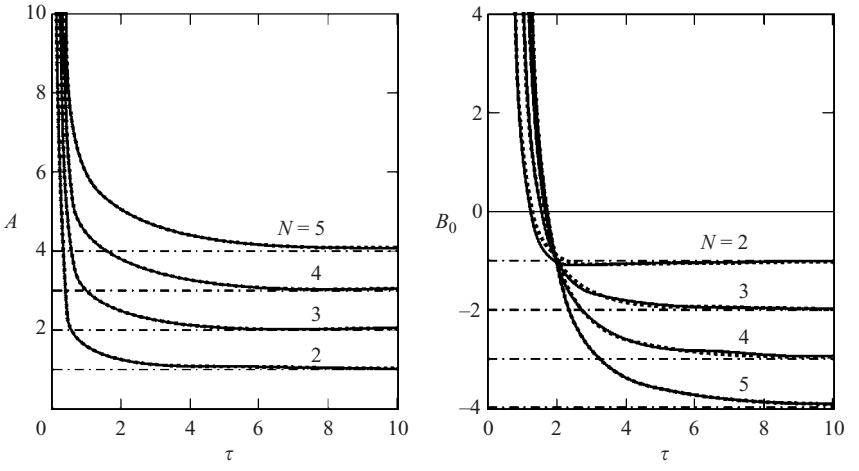

FIGURE 3. Computed co-factors A and B_0 (without assigned flow) as a function of vortex pitch τ, for $s=1$ and various values of N, based on exact solution (——) and on a solution without remainder terms (·····).

$$+\frac{4\left(1-\tau^2\right)}{\tau^3}\sum_{m=1}^{\infty}\left[\left(m\,ri_m^{0,1}\left(\frac{1}{\tau},\frac{1}{\tau}\right)\right)\left(1+\sum_{n=0}^{N-1}\cos\left(2\pi\frac{nm}{N}\right)\right)\right]$$
$$+\frac{4\left(1+\tau^2\right)^2}{\tau^4}\sum_{m=1}^{\infty}\left[m^2\,ri_m^{0,0}\left(\frac{1}{\tau},\frac{1}{\tau}\right)\left(1+\sum_{n=0}^{N-1}\exp\left(2\pi\mathrm{i}\frac{ns}{N}\right)\cos\left(2\pi\frac{nm}{N}\right)\right)\right]. \tag{2.18}$$

In figure 3 the behaviour of B_0 is shown for different helical multiples in free space. It is seen that, depending on the value of the pitch τ, the vortex system may be either stable or unstable. For τ-values less than about 1.6 the system is always unstable if $N \geqslant 2$. Note that in the limit $\tau \to \infty$, A and B_0 tend to the point vortex solution

$$4\pi a A/\Gamma = s(N-s) \text{ and } 4\pi a^2 B_0/\Gamma = s(N-s) - 2(N-1),$$

described by Havelock (1931). The asymptotic levels for A and B_0 are indicated by horizontal dot-dash lines in the plots. In the figures calculations of A and B_0 are also shown without the regular remainders in equations (2.12)–(2.14) and (2.16). Note that analysing the asymptotic solution at $\tau \to \infty$ helps to define the most unstable modes for s by taking the value closest to $N/2$, i.e. $s^* = N/2$ for even N and $s^* = (N \pm 1)/2$ for odd N. In the following only the principal wavenumbers are used to estimate the unstable regions.

In the next section we consider the influence of different assigned flows on the equilibrium properties of the helical multiple. First, however, we evaluate how the regular reminders and the derivative of the self-induced motion described by (2.16) influence the stability properties of B_0. In order to do this, calculations of B_0-neutral curves are repeated and compared in figure 4 with and without the terms in (2.16). In the figure the computations are further compared to figure 7 in Okulov (2004). From figures 3 and 4 it is seen that neglecting the terms of the regular reminders only has a limited influence on the stability properties, hence these terms may be omitted.

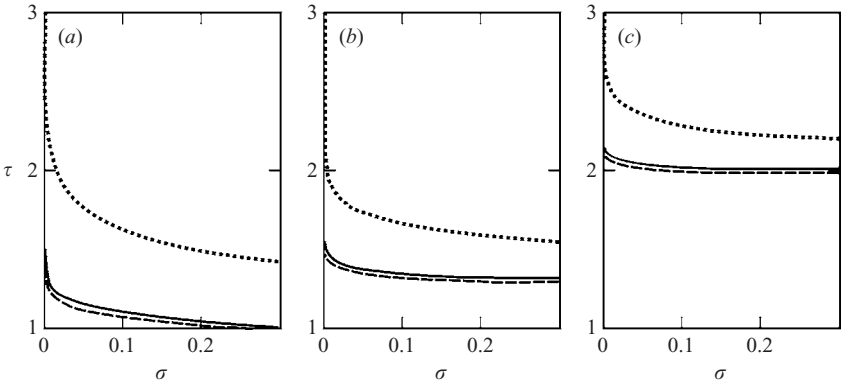

FIGURE 4. Neutral stability curves (stable region above each curve) for equilibrium of a pair (*a*), triplet (*b*) and quartet (*c*) of helical vortices based on exact solution (——) and on a solution without remainder terms (– – –). Data of Okulov (2004) are indicated by ·····.

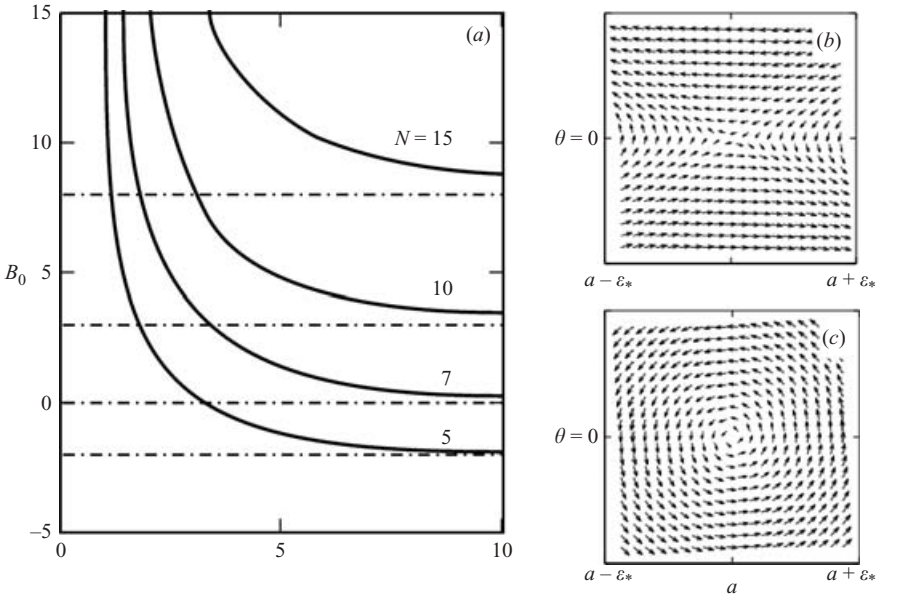

FIGURE 5. Examples of B_0 (without assigned flow) for multiple helical vortices (*a*) and corresponding relative velocity plots about the vortex axis for (*b*) unstable and (*c*) stable critical points.

In contrast to this, the influence of a change in the self-induction movement of the vortices cannot be completely neglected, as clearly illustrated by figure 4.

Figure 5 explains the physical meaning of vortex equilibrium instability when B_0 becomes positive. Here planar velocity plots in the vicinity of the vortex centre from an array of rotating vortices in equilibrium is reproduced for $B_0 < 0$ ($N = 5,\ s = 3,\ \tau \to \infty$) and $B_0 > 0$ ($N = 15,\ s = 3,\ \tau \to \infty$). In the first case the velocity field at the vortex position has a stable critical point (velocity plot *c*) and for the second one the point is unstable (velocity plot *b*). Note also that a multiple consisting of seven helical vortices is unstable for all finite pitch values with $B_0 > 0$, and only at $\tau \to \infty$, where

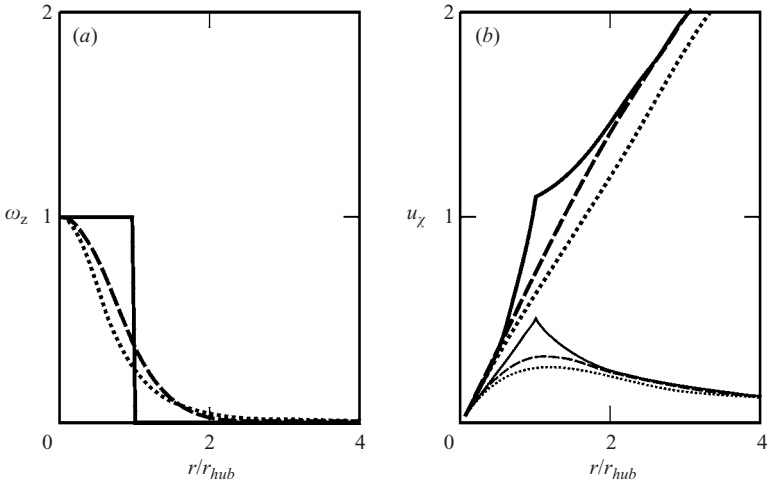

FIGURE 6. Examples of assigned flows with different axial vorticity distributions: Rankine (——), Lamb (– – –) and Scully (· · · ·) types. (*b*) Helical velocity component: thick lines correspond to $\tau_{hub} = 1$ and thin lines to $\tau_{hub} \to \infty$.

the problem is reduced to the stability of an array of point vortices, is the system neutrally stable with $B_0 = 0$, according to Kurakin & Yudovich (2002).

3. Parametrical study of stability condition

In the previous section we tested the stability of multiple helical vortices subject only to induced and self-induced actions without an assigned velocity field, i.e. with the last term in the definition of B, equation (2.17), set equal to zero. In this section we investigate the conditions for linear stability to infinitesimally small space displacements of a multiplicity of helical vortices embedded in an assigned flow field. It is implicitly assumed that the vortices do not influence the assigned flow field.

As examples of assigned flows, different types of axisymmetric columnar helical vortices of finite core size having their axes coinciding with the multiple axis oz will be considered in the following. Since the axial component of velocity is connected to the azimuthal velocity by (2.8), and introducing the vorticity components $\omega_r = 0$ and $\omega_\theta = r\,\omega_z / l$ with the helical pitch l, the expression for the assigned velocity field is written as

$$(u_0)_\theta = \frac{1}{r}\int_0^r \omega_z(r) r\,\mathrm{d}r, \quad (u_0)_z = V_\infty - \frac{1}{l_{hub}}\int_0^r \omega_z(r) r\,\mathrm{d}r, \quad V_\infty = \text{const}, \tag{3.1}$$

where $\omega_z(r)$ is the axial vorticity distribution along the columnar vortex core and V_∞ defines the translational motion of the total vortex system.

Within the framework of the proposed inviscid flow model, it is possible to choose an arbitrary vorticity distribution in the vortex core (Kuibin & Okulov 1996; Alekseenko *et al.* 1999). There are three important examples of columnar vortices with a simple distribution of axial vorticity in a cylindrical core of effective radius r_{hub} (figure 6*a*):

$$\omega_z = \frac{\Gamma_0}{\pi r_{hub}^2}\begin{cases}1, & r \leqslant r_{hub}\\ 0, & r > r_{hub},\end{cases} \qquad \omega_z = \frac{\Gamma_0}{\pi r_{hub}^2}\exp\left(-\frac{r^2}{r_{hub}^2}\right) \qquad \omega_z = \frac{\Gamma_0}{\pi r_{hub}^2}\left(1+\frac{r^2}{r_{hub}^2}\right)^{-2}, \tag{3.2}$$

where Γ_0 is the circulation of the assigned flow field. In the two-dimensional case, where $l \to \infty$ and $\omega_\theta \to 0$, these vortices correspond to Rankine, Lamb and Scully vortices, respectively (Hopfinger & van Heijst 1993; Scully 1975). In the following they are referred to as *R*-, *L*- and *S*-vortices, respectively. The *R*-model consists of a step-shape vorticity distribution, which is a rather crude model that can only be applied as a first-order approximation of a real vortex core. As seen from figure 6, the *L*- and *S*-vortices are very similar, the main difference being that the *S*-vortex is described by a polynomial whereas the vorticity distribution of the *L*-vortex is Gaussian. Comparing the vorticity distributions with measured data shows that the *L*-vortex fits laminar velocity profiles well whereas the *S*-vortex is a suitable approximation for turbulent vortices (see Murakhtina & Okulov 2000; Martemianov & Okulov 2004).

From (3.1), (3.2) and (2.8) the helical velocity components for the three distributions of assigned hub vorticity are written as, respectively,

$$u_{0\chi} = \frac{\Gamma_0}{2\pi r}\left(1+\frac{r^2}{l^2}\right)\begin{Bmatrix} r^2/r_{hub}^2, & r \leqslant r_{hub} \\ 1, & r > r_{hub} \end{Bmatrix} + V_\infty \frac{r}{l}, \tag{3.3a}$$

$$u_{0\chi} = \frac{\Gamma_0}{2\pi r}\left(1+\frac{r^2}{l^2}\right)\left[1-\exp\left(-\frac{r^2}{r_{hub}^2}\right)\right] + V_\infty \frac{r}{l}, \tag{3.3b}$$

$$u_{0\chi} = \frac{\Gamma_0}{2\pi r}\left(1+\frac{r^2}{l^2}\right)\frac{r^2}{r^2+r_{hub}^2} + V_\infty \frac{r}{l}, \tag{3.3c}$$

Figure 6(*b*) shows the behaviour of the helical velocity component $u_{0\chi}$ with $\Gamma_0 = 2\pi$ and $V_\infty = 0$ for finite helical pitch $l/r_{hub} = 1$ (thick lines) and infinite helical pitch $l \to \infty$ (thin lines).

To establish a connection between the properties of the helical vortices and the assigned flow we introduce the circulation ratio $\gamma = \Gamma_0/N\Gamma$, which is the strength of the hub vortex divided by the total circulation of the multiple, and the relative size of the hub vortex, $\delta = r_{hub}/a$, which is the core radius of the hub vortex normalized by the radius of the vortex multiple. The dimensionless hub-vortex pitch $\tau = l/a$ is assumed to keep the same value as that of the multiple. The last term of B given below (2.17) describes the influence of the assigned velocity field. Introducing (3.3*a*)–(3.3*c*), depending on the type of assigned flow field, this term takes the dimensionless forms:

R-type vorticity distribution

$$B_A(N,\tau,\delta,\gamma) = \frac{4\pi a^2}{\Gamma}\left(\frac{\mathrm{d}}{\mathrm{d}r}u_{0\chi} - \frac{u_{0\chi}}{a}\right) = 4N\gamma\begin{cases} -1, & \delta < 1 \\ 1/\tau^2\delta^2, & \delta \geqslant 1, \end{cases} \tag{3.4a}$$

L-type vorticity distribution

$$B_A(N,\tau,\delta,\gamma) = \frac{4\pi a^2}{\Gamma}\left(\frac{\mathrm{d}}{\mathrm{d}r}u_{0\chi} - \frac{u_{0\chi}}{a}\right) = 4N\gamma\left[\left(\frac{1+\tau^2}{\delta^2\tau^2}+1\right)\exp\left(-\frac{1}{\delta^2}\right)-1\right], \tag{3.4b}$$

S-type vorticity distribution

$$B_A(N,\tau,\delta,\gamma) = \frac{4\pi a^2}{\Gamma}\left(\frac{\mathrm{d}}{\mathrm{d}r}u_{0\chi} - \frac{u_{0\chi}}{a}\right) = 4N\gamma\frac{1}{1+\delta^2}\left[\frac{1+\tau^2}{\tau^2}\frac{\delta^2}{1+\delta^2}-1\right]. \tag{3.4c}$$

Note that, irrespective of flow type, B_A does not contain any term with V_∞, implying that the translational motion does not influence the stability. In figure 7, B_A is compared for all three assigned vorticity fields for $\tau = 1$ (thick lines) and $\tau = \infty$ (thin lines).

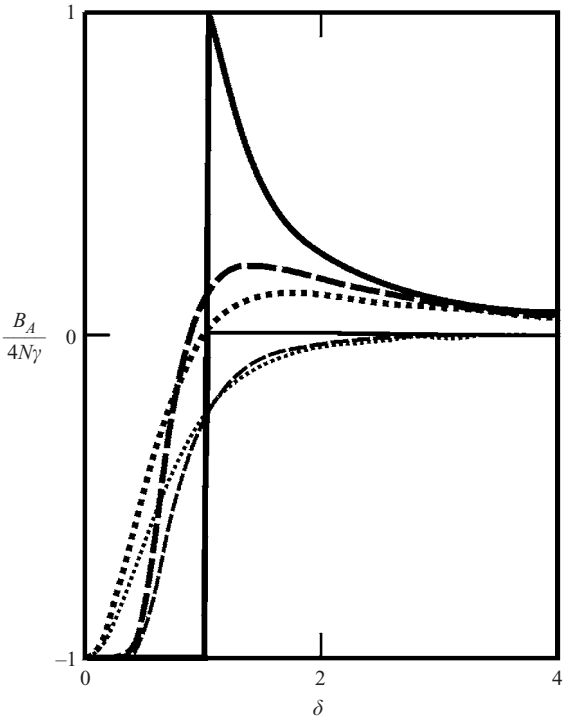

FIGURE 7. Dependence of contribution B_A of an assigned flows on effective radius δ for different axial vorticity distributions: Rankine (———), Lamb (– – –) and Scully (· · · ·) types. Thick lines correspond to $\tau_{hub} = 1$ and thin lines to $\tau_{hub} \to \infty$.

Substituting B_0 from (2.18) and B_A from (3.4*a*)–(3.4*c*) in the definition of B, given below (2.17), the stability conditions are governed by the correlation equation

$$B(N, s, \tau, \sigma, \delta, \gamma) \equiv B_0(N, s, \tau, \sigma) + B(N, \tau, \delta, \gamma) = 0. \tag{3.5}$$

The equation shows how the stability problem depends on the parameters $\{N, s, \tau, \sigma, \delta, \gamma\}$.

In the following we analyse the stability properties of multiples of helical vortices $\Lambda^{\pm}$ with different numbers of vortices N and values of the core size δ, as a function of helical pitch τ and circulation ratio γ for the three assigned flow fields. The most unstable mode is taken as the subharmonic wavenumber, s, that is closest to $N/2$. For simplicity, the core radius is fixed at $\sigma = 0.05$. In figures 7–12 stable regions are located on the side of the neutral curves with the darkest shading.

3.1. *Stability analysis for vortices embedded in an assigned flow of R-type*

As seen from figure 7 there exist two ranges of B_A depending on whether the hub vortex lies inside ($\delta < 1$ or $r_{hub} < a$) or outside ($\delta \geqslant 1$ or $r_{hub} \geqslant a$) the surface formed by the helical vortices.

In the first range ($0 \leqslant \delta < 1$), $B_A/4N\gamma = -1$, independent of the value of the helical pitch τ. Thus, in this region the stability limit is the same for all internal hub vortices, independent of the size of the core radius. Plots (*a*) of figures 8–10 show neutral stability curves for a pair of helical vortices (figure 8*a*), and for multiple helical vortices with $N < 7$ (figure 9*a*) and $N \geqslant 7$ (figure 10*a*). The vortex configuration is unconditionally unstable for small values of the helical pitch τ and for most of the

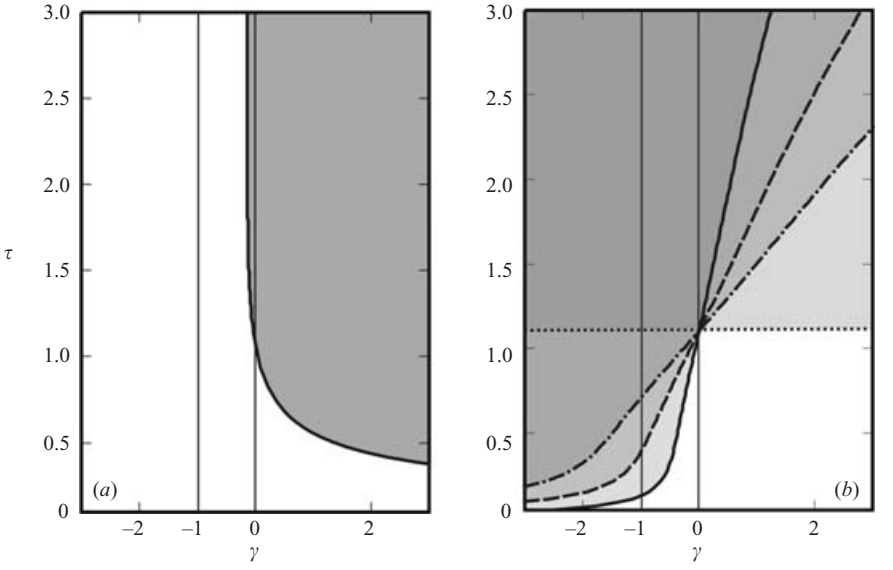

FIGURE 8. Neutral stability curves for a pair of helical vortices ($N = 2$) embedded in an R-type flow with different size of hub vortex core. Stable regions are located on the side of the curve with the darkest shading. (*a*) $0 \leqslant \delta \leqslant 1$ (——); (*b*) $\delta = 1$ (——), 1.5 (– – –), 2 (– · –), 50 (· · · · · ·).

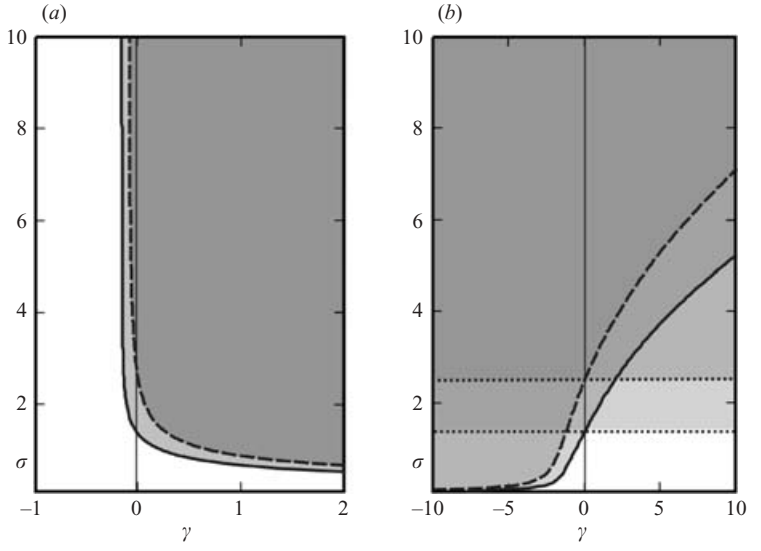

FIGURE 9. Neutral stability curves for multiple helical vortices with $N < 7$: $N = 3$ (——) and 5 (– – –) embedded in an R-type flow with different size of hub vortex core. Stable regions are located on the side of the curve with the darkest shading. (*a*) $\sigma \leqslant \delta \leqslant 1$; (*b*) $\delta = 1.5$ and 50 (· · · · · · for both multiples).

negative values of γ, including the important case $\gamma = -1$ where the total circulation of the vortex configuration is zero. For $N < 7$ stable states may exist for $0 > \gamma > -1$. For $\tau \to \infty$ the stability limit is given as

$$\gamma_\infty = [s(N - s) - 2(N - 1)]/4N. \tag{3.6}$$

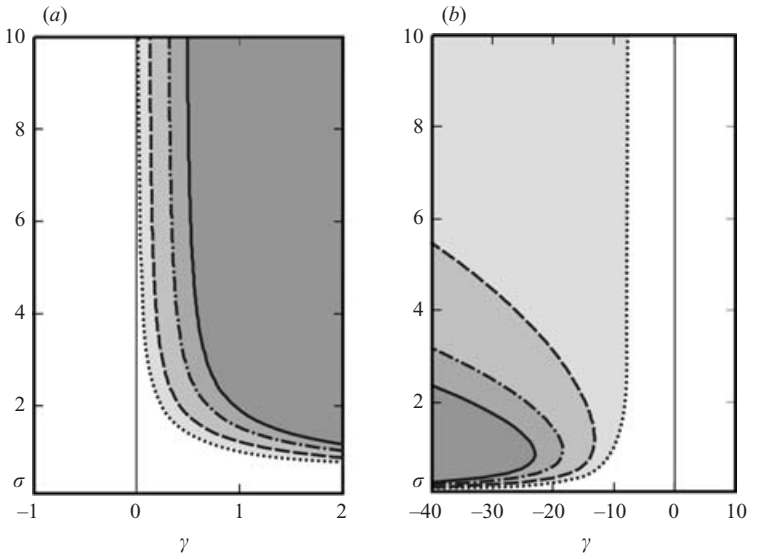

FIGURE 10. Neutral stability curves for multiple helical vortices with $N > 7$: $N = 7$ (·····), 9 (– – –), 12 (– · – ·), 15 (——) embedded in an R-type flow with different size of hub vortex core. Stable regions are located on the side of the curve with the darkest shading. (*a*) $0 \leqslant \delta \leqslant 1$ and (*b*) $\delta = 3$.

N	2	3	4	5	6	7	8	9	10	11	12	13	14	15
γ_∞	$-\frac{1}{8}$	$-\frac{1}{6}$	$-\frac{1}{8}$	$-\frac{1}{10}$	$-\frac{1}{24}$	0	$\frac{1}{16}$	$\frac{1}{9}$	$\frac{7}{40}$	$\frac{5}{22}$	$\frac{7}{24}$	$\frac{9}{26}$	$\frac{23}{56}$	$\frac{7}{15}$

TABLE 1. γ-stability limits at $\tau \to \infty$ for R-type hub vorticity distribution with $\delta < 1$.

These values are given in table 1. Note that (3.6) is identical to the stability limit of an $(N + 1)$-system consisting of N point vortices in a circular array and a centre vortex, found by Morikawa & Swenson (1971). However, they mistakenly wrote that the stability limit becomes infinite for $N = 2$ and 3.

In the second case, where $\delta \geqslant 1$, $B_A(\delta)$ is a decreasing positive function for all finite helical pitch values τ. Further, $B_A(\delta)$ tends to zero for $\delta \to \infty$, that is when the assigned flow rotates as rigid body, and for an infinite pitch $\tau \to \infty$, that is when the multiple turns into a circular array of point vortices. This means that the condition for stability of a circular array of point vortices embedded in a flow field rotating like a rigid body takes the same form as the condition for a vortex system in free space without hub vorticity (Havelock 1931). Examples of stability regions for a pair of helical vortices with finite pitch are presented in figure 8(*b*) for different values of δ. Unlike the first case with internal hub vortex core, B_A changes sign and the vortex configuration becomes stable for most of the negative values of γ, including the case $\gamma = -1$, where the total circulation of the vortex configuration is zero. At $\delta = 1$ the unstable zone decreases when τ increases and the stable zone expands to all values of γ when $\tau \to \infty$, in accordance with Havelock's analysis for a system of point vortices. On increasing δ the neutral curves 'turns' around the point ($\gamma = 0$, $\tau = \tau_0$), implying that neutral stability is always achieved for multiple vortices in free space. The values of τ_0 as a function of the number of helical vortices are given in table 2. In the

N	2	3	4	5	6
τ_0	1.106	1.132	2.019	2.481	4.310

TABLE 2. Neutral points for multiple stability in free space ($\gamma = 0$).

N	2	3	4	5	6
δ_0	0.955	1.106	1.536	1.845	3.101
δ_*	1.491	1.682	2.253	2.675	4.423
γ_∞	−0.417	−0.844	−1.837	−2.811	−8.255

TABLE 3. Stability characteristics for *S*-type hub vorticity distribution.

N	2	3	4	5	6
δ_0	1.106	1.132	2.019	2.481	4.310
δ_*	1.856	2.157	3.025	3.649	6.176
γ_∞	−0.617	−1.333	−3.222	−5.122	−15.96

TABLE 4. Stability characteristics for *L*-type hub vorticity distribution.

limiting case $\delta \to \infty$, where the space is a rotating rigid body, the helix couple is stable for all γ when $\tau \geqslant \tau_0$.

It is remarkable that, as in the case of a circular array of point vortices (Havelock 1931), the stability problem of a system of helical vortices with $N = 7$ has to be considered as a special case. Indeed, the stability properties of multiples with $N < 7$are quite different from multiples with $N > 7$. For $N < 7$ (figure 9*b*) the behaviour of the neutral stability curves is similar to that for a pair of vortices. A distinction between the various numbers of vortices ($2 \leqslant N < 7$) may be found in the different values of the neutral point τ (see table 2). For $N > 7$ (figure 10*b*) the unstable zone increases with growing τ and expands to all values of γ when $\tau \to \infty$, in accordance with Havelock's finding for point vortex systems with $N > 7$.

3.2. *Stability analysis for vortices embedded in assigned flows of L- and S-type*

For *L*- or *S*-type vorticity distributions it is not possible to distinguish between internal and external multiples, since the hub vorticity has non-zero values up to infinity (figure 6*a*). Essential features of the function B_A are shown in figure 7. The general behaviour is that $B_A(\delta)$ increases from a negative value at $\delta = 0$ to a maximum value at $\delta = \delta_*$, after which it decreases monotonically to zero for $\delta \to \infty$. Further, B_A shifts sign from negative to positive at $\delta = \delta_0$. The values of δ_0, δ^* and γ_∞, as a function of the number of blades, are given in tables 3 and 4.

For both *L*- and *S*-type vorticity distributions an additional stable region, which disappears for small δ-values, is found in the left bottom part of the plots in figures 11(*a*) and 11(*b*) for $\delta < \delta_0$. It is noteworthy that the two stable regions are disconnected for $\delta < \delta_0$ and that the neutral stability curves merge when $\delta = \delta_0$. In the figures the horizontal lines define the neutral values of τ_0 for stability of multiples in free space when $\gamma = 0$ (see also table 2).

Comparing the stability curves of figure 8(*a*) with those of figures 11(*a*) and 11(*b*) it is seen that the stability properties for small δ-values are very similar for the three types of vorticity distributions. This is readily explained from figure 7 where the value of $B_A/4N\gamma$ for all cases is close to –1.

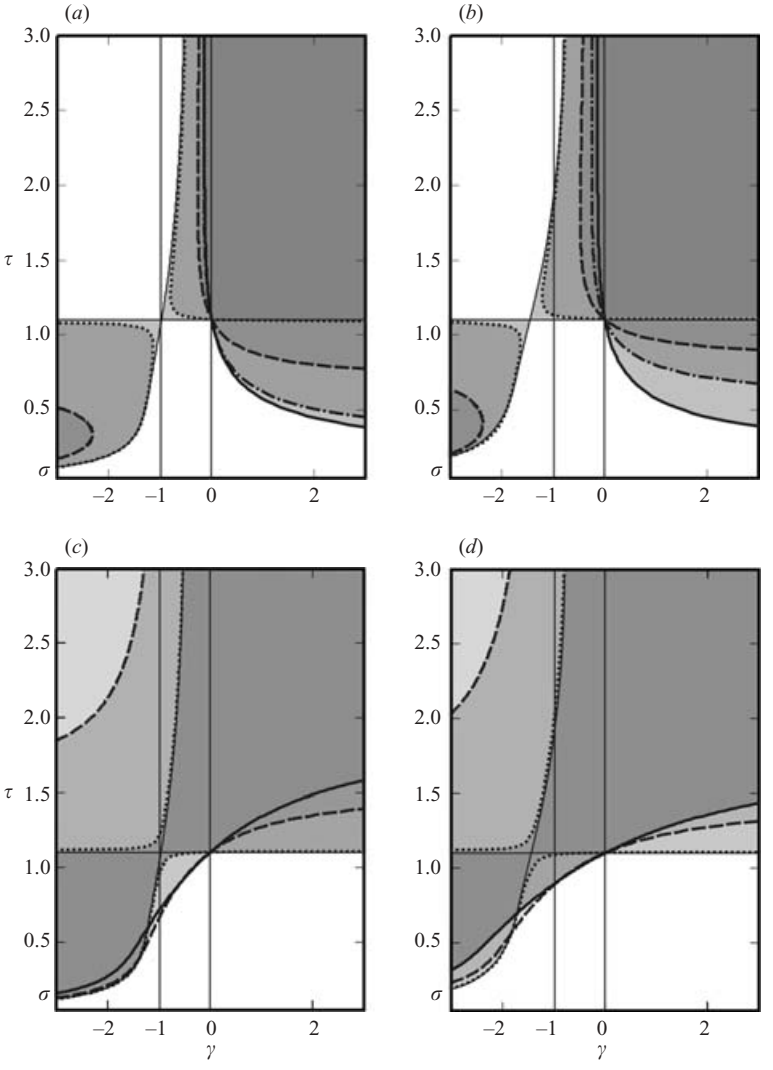

FIGURE 11. Neutral stability curves for a pair of helical vortices ($N=2$) embedded in (a, c) L- and (b, d) S-type flows with different size of the hub vortex core (with values δ_0 and δ_* from tables 2 and 3). Stable regions are located on the side of the curve with the darkest shading. (a, b) $\delta=\sigma$ (——), $0.5\delta_0$ (–·–·), $0.75\delta_0$ (– – –), $0.99\delta_0$, and δ_0 (——); (c, d) $\delta=\delta_0$ (——), $\delta_0+0.1(\delta_*-\delta_0)$ (·····), $\delta_0+0.5(\delta_*-\delta_0)$ (– – –), and δ_*(——).

The next state of stability appears when $\delta_0<\delta<\delta_*$. Figures 11(c) and 11(d) show that the area of stability now has become singly-connected and that it grows in size when δ increases. For $\delta\geqslant\delta_*$, $B_A(\delta)$ is a decreasing positive function that tends to zero for $\delta\to\infty$ and becomes identically equal to zero for an infinite value of the pitch τ. The behaviour of $B_A(\delta)$ is in this case similar for the three vortex types and the stability regions for L- and S-type vortices are similar to that for R-type assigned flow. For increasing δ-values the upper branch of the neutral stability curves disappears and the lower ones 'turn' around the neutral point τ_0 of the pair stability in free space (table 2) to achieve a limiting case at $\delta\to\infty$, when all space is rotating like a rigid body and the helical pair is stable for all γ if $\tau\geqslant\tau_0$.

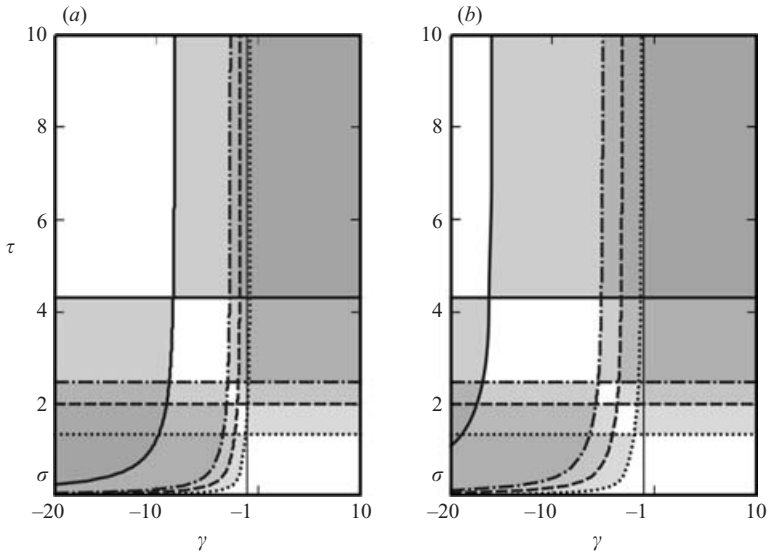

FIGURE 12. Neutral stability curves for multiple helical vortices with $N < 7$: $N = 3$ (·····), 4 (– – –), 5 (– · – ·), and 6 (——) embedded in (*a*) *L*- and (*b*) *S*-type flows at $\delta = \delta_0$. Stable regions are located on the side of the curve with the darkest shading.

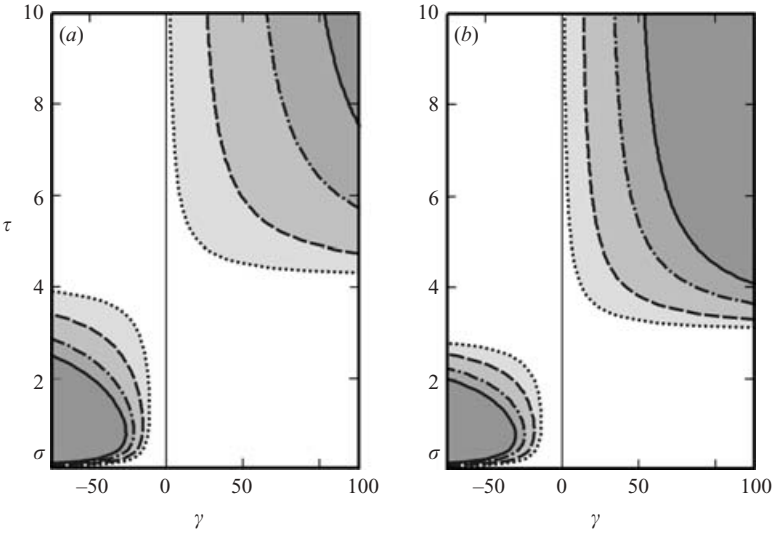

FIGURE 13. Neutral stability curves for multiple helical vortices with $N > 7$: $N = 7$ (·····), 9 (– – –), 12 (– · – ·), 15 (——) embedded in (*a*) *L*- and (*b*) *S*-type flows at $\delta = 3$. Stable regions are located on the side of the curve with the darkest shading.

To analyse the influence of the number of vortices we put $\delta = \delta_0$ for simplicity and predict the limit neutral stability curves when the two stable regions merge. Again two different cases have to be considered. For $N < 7$ the stability regions correspond qualitatively to those obtained for a pair of vortices, as described above. This is seen in figure 12 that displays the neutral stability curves for $\delta = \delta_0$ and for $N = 3$, 4, 5, and 6. For $N \geqslant 7$, however, the behaviour of the stability curves is quite different. As seen from figure 13 the stability regions are now divided into two non-connected areas which disperse at increasing N.

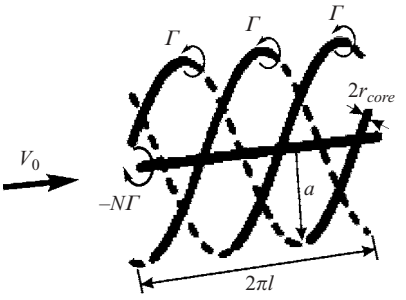

FIGURE 14. Sketch of the far-wake model proposed by Joukowski (1912).

For $\tau \to \infty$ the stability curve becomes independent of the pitch and limited by the following expressions for γ:

$$\gamma_\infty = \frac{\delta^2}{4N} \frac{s(N-s) - 2(N-1)}{\delta^2 - (1+\delta^2)\exp(-1/\delta^2)}, \tag{3.7a}$$

$$\gamma_\infty = \frac{s(N-s) - 2(N-1)}{4N(1+\delta^2)^2}, \tag{3.7b}$$

for L- and S-type flows, respectively. Note that the limit values (3.7a) and (3.7b) differ from the limit values given by (3.6) for the R-type case by a factor that only depends on δ.

Comparing the stability properties of the various types of hub vortices, it is noted that the stability properties of helical multiples embedded in a hub vortex of L- or S-type at $\delta = o(0)$ and $\delta \gg 1$ are close to those embedded in a vortex of R-type. This is most easily seen by comparing the B_A-functions in figure 7. A distinct feature of the R-type hub vortex, however, is that it is associated with discontinuous stability properties due to the stepwise change in the sign of B_A at $\delta = 1$. Comparing plots (a) and (b) in figures 8–10 the discontinuous stability behaviour is seen to result in two markedly different areas of stability, depending on whether $B_A < 0$ or $B_A > 0$. In contrast to this, both S- and L-type hub vortices exhibit continuous stability features, as seen in figures 11–13. Comparing the figures, it is found that the stability properties of the L- and S-type hub vortices for $\delta = o(1)$ are generally quite different from those of the R-type hub vortex, but that the stability behaviour of the L- and S-type vortices corresponds to that of the R-type at small and large δ-values. Further, it may be noted that the L-type hub vortex generally exhibits better stability properties than the corresponding S-type hub vortex.

4. Application of the analysis

In 1912 Joukowski proposed a simple model for a two-bladed propeller that basically consists of two rotating horseshoe vortices, corresponding to the tip and root vortices created by the rotation of the propeller blades. The tip vortices are represented by helical vortices of strength Γ and the root or hub vortex is represented by an axial vortex of strength $\Gamma_0 = -2\Gamma$, in order to conserve circulation. In the far wake behind the rotor plane the flow is described by infinitely long helical vortices with constant pitch and radius (see figure 14). Based on this model the self-induced motion of the helical tip vortices was investigated. From a historical point of view it is interesting to note that Joukowski (1912) was the first to exploit the Biot-Savart

integral to prove that the self-induced velocity of a helix may be evaluated roughly via the self-induced velocity of an osculating vortex ring.

The first fundamental analysis of the linear stability of multiple helical vortices was carried out by Gupta & Loewy (1974) who, using a numerical cutoff approximation, extended the stability analysis by Levy & Forsdyke (1928) and Widnall (1972) for centreline perturbations of a single helical vortex. Gupta & Loewy (1974) simulated the far wake behind the rotor as multiple helical vortices and found it to be inherently unstable with many possible instability modes. It should be noted, however, that most of the results of Gupta & Loewy were calculated at a pitch value $\tau = 0.1$ and a vortex core of radius $\sigma = 0.1$ or 0.33. A similar conclusion was given by Okulov (2004) in the first analytically obtained solution to the problem (see figure 4). Indeed, the neutral stability curves for all N-multiples and values of the vortex core lie in the region $\tau > 1$, meaning that instability occurs for all smaller pitch values, including the cases treated by Gupta & Loewy. An interesting feature of the stability problem is that it seems not to depend on the type of disturbance introduced: in the analysis of Gupta & Loewy (1974) a sinusoidal disturbance was introduced whereas a constant spatial displacement was employed by Okulov (2004). The reason is readily explained by inspection of the velocity plots in figures 5(*b*) and 5(*c*). Here arbitrary infinitesimal perturbations of the helix centre from its equilibrium in free space results in instability when the relative velocity distribution describes an unstable critical point (figure 5*b*), whereas perturbations damp out when the velocity distribution describes a stable critical point (figure 5*c*).

Unfortunately the conclusions concern the stability of helical multiples in free space only. If we return to Joukowski's far-wake model with a concentrated root vortex (figure 14) we find that the tip vortex system is unconditionally unstable for all pitch values (see plots *a* of figures 8, 9 and 10 for $\gamma = -1$). It may be noted that this important conclusion is the result of an exact analysis, involving all dominant terms, whereas our previous conclusion about the possibility of conditional stability for Joukowski's model (Okulov & Sorensen, 2004*a*, *b*) was due to an approximate approach in which we neglected the derivatives of the self-induced motion, described by (2.16), and the assigned flow defined by the first term in the definition of B_A in (3.4). On the other hand, our conclusion about the unconditional instability of Joukowski's model seems to be in conflict with numerous visualizations of rotor wakes showing that helical tip vortices, even with small pitch values, can be stable (see e.g. Vermeer *et al.* 2003).

The most likely explanation for this apparent contradiction is that the model of Joukowski is too simplified to describe the general behaviour of rotor flows. Joukowski's model is based on the assumption that the circulation is constant over the blade span, and that the wake only consists of a root vortex and trailing tip vortices. Considering the non-constant circulation that usually characterizes the operating range of a rotor, trailing vortices are created behind the rotor blades. These vortices form a helical vortex sheet or screw surface along with the strong tip vortices. After the vortex sheet and the tip vortices are formed behind the rotor, a complicated roll-up process starts to take place due to the mutual influence between the vortices. It is likely that this process will eventually divide the flow field into strong, distinct helical tip vortices and a more or less compact centre vortex with a core size of up to a rotor radius (see e.g. Landgrebe 1972 and Vermeer *et al.* 2003). This behaviour is schematically shown in figure 15 where it is illustrated how the mixing of the wake behind a propeller may result in the formation of an axial centre vortex with distinct embedded tip vortices.

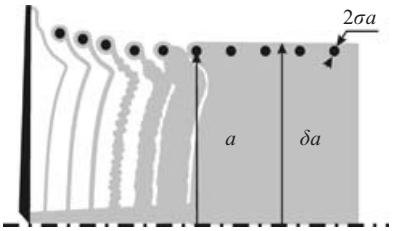

FIGURE 15. Sketch of vorticity distribution in a meridional cross-section of the rotor wake for the present model of a far wake with uniform distribution of hub vorticity.

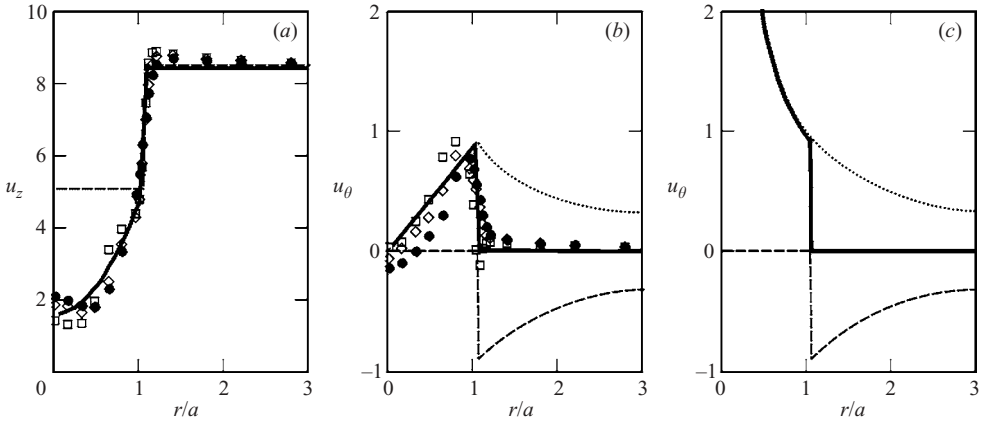

FIGURE 16. Comparison between measured and simulated azimuthally averaged velocity distributions: (*a*) axial velocity profiles; (*b*) azimuthal velocity profiles; (*c*) azimuthal velocity profiles computed by Joukowski's model. – – –, velocity profiles induced by tip vortices without hub vorticity; · · · · · ·, velocity profiles induced by hub vorticity; ——, velocity profiles induced by tip vortices and hub vorticity; experimental data by Medici & Alfredsson (2004) at cross-section from rotor plane: $x/a = 2.8(\square); 3.8(\diamond); 4.8(\bullet)$.

The new far-wake model outlined was inspired by the above-mentioned visualizations. To validate the model, it is compared to the experimental data by Medici & Alfredsson (2004) who measured velocity distributions at various cross-sections in the wake of a two-bladed rotor in a wind tunnel. The parameters of the vortex system were set as follows: $N = 2$, $\gamma = -1$, $\delta = 1.05$ and $\sigma = 0.05$; with the tip vortices defined as multiple left-handed helical vortices. Thus, for the comparison, we assume that the total circulation is zero ($\sum \Gamma = \Gamma_0 + N\Gamma = 0$) and that the core size of the tip vortices corresponds to 5% of the wake radius. This is merely a guess, which, however, has no visible influence on the final result. As we do not know the actual loading, we assume, as depicted in figure 15, that the root vortex has merged with the shed vorticity in the wake, forming a continuous distribution of vorticity. This is modelled as a Rankine vortex of radial extent $\delta = 1.05$. The remaining parameters, i.e. the circulation of the tip vortices Γ and the pitch τ, were finally determined by fitting the model to the experimental data. The comparison is shown in figures 16(*a*) and 16(*b*) where azimuthally averaged velocity distributions are compared at a cross-section corresponding to 3.8 rotor radii downstream from the rotor plane. As seen in figure 16(*a*), the inclusion of a distributed centre vortex results in an axial velocity distribution in very good agreement with measured data. The values used for the comparison are $\Gamma = -3$ and $\tau = 0.28$. The corresponding azimuthal

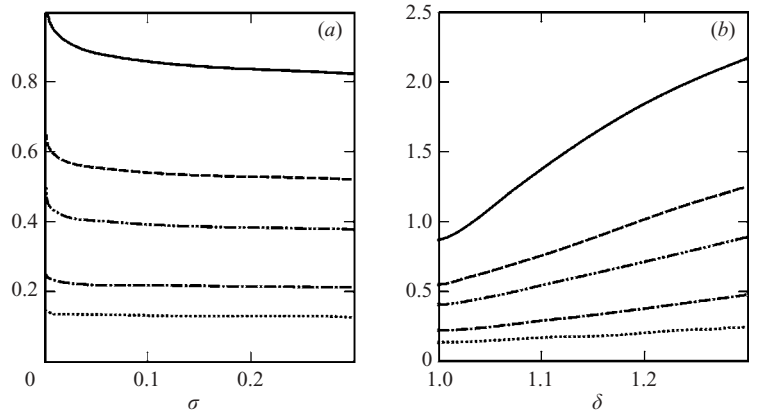

FIGURE 17. Neutral stability curves (stable region above each curve) for equilibrium of multiple helical vortices $N=2$ ($\cdots\cdots$); 3 ($-\cdot-\cdot$); 4 ($-\cdot\cdot-$); 5 ($---$) and 6 (——) in an assigned flow with R-vorticity distribution and circulation $\Gamma_0=-N\Gamma$ ($\gamma=-1$). (*a*) as a function of vortex radius σ for $\delta=1.05$ and (*b*) as a function of the radius of the hub vorticity δ for $\sigma=0.05$.

velocity distribution is shown in figure 16(*b*). Since the centre vortex is modelled by a Rankine vortex the resulting azimuthal velocity profile is linear, corresponding to solid body rotation in the wake and zero outside the wake. The comparison shows that there is excellent agreement between the modelled behaviour and the measurements. To illustrate the behaviour of a root vortex of zero extent ($\delta\approx 0$), corresponding to the original model of Joukowski, one would obtain a $v_\theta=\text{const}/r$ dependence, as shown in figure 16(*c*). This is clearly in contradiction to the measured behaviour.

To derive more general stability properties we keep $\gamma=-1$ and vary σ, δ and N. The outcome is shown in figure 17 which depicts curves of neutral stability, $\tau=\tau(\sigma,\delta,N)$. In figure 17(*a*) curves for neutral stability, $\tau=\tau(\sigma)$, for $\delta=1.05$ and at different numbers of blades are shown, $N=2, 3, ..., 6$, and in figure 17(*b*) stability curves, $\tau=\tau(\delta)$, are shown for $\sigma=0.05$. From the figures it can be concluded that an increase in the core radius of the hub vortex leads to loss of stability, whereas an increase in the size of the tip vortices leads to a more stable vortex system. A comparison with the measured data of Medici & Alfredsson (2004) shows that the best fit is found for $\tau=0.28$. Since the considered rotor is two-bladed ($N=2$), in accordance with the experimental data, we find that the tip vortices in this case form a stable system. The actual core size of the tip vortices and the size of the hub vortex will of course depend on the loading on the blades.

5. Conclusion

The classical problem of the stability of multiple helical vortices has been generalized to include vortices embedded in an assigned flow field. This vortex system, which is an extension of the model of Joukowski (1912), consists of helical tip vortices embedded in a helical vortex field formed by the trailing vortex sheet of the blades and the root vortices. In contrast to the model of Joukowski, the new model explains the existence of stable tip vortices.

Analytical solutions of the stability problem have been derived for three different assigned flows, consisting of axisymmetric helical vortices with uniform-, polynomial- and Gaussian-distributions of axial vorticity. The models show that the stability of

helical vortices embedded in an assigned flow depends strongly on the radial extent of the assigned vorticity field. New regions of stability were found for multiple helical vortices subject to small pitch values.

Comparison with experiments (Medici & Alfredsson 2004) shows that the considered vortex model gives an excellent representation of the far wake behind a wind turbine. The vortex model is used as the basic flow model for predicting stability boundaries of far wakes behind multi-bladed rotors. As an intermediate result of the analysis it is demonstrated that representing the far wake by N tip helical vortices and a slender root vortex results in unconditionally unstable flow behaviour. However, introducing an assigned vorticity distribution that corresponds to the measurements stabilizes the tip vortices and explains the existence of experimentally observed stable wake structures.

The work was supported by the Danish Energy Agency under the project "Dynamic wake modeling" (grant 33030-0004), Danish Research Agency (grant 2104-04-0005) and the Russian Foundation for Basic Research under grant 04-01-00124. The authors thank David Medici for providing the experimental data.

REFERENCES

Alekseenko, S. V., Kuibin, P. A., Okulov, V. L. & Shtork, S. I. 1999 Helical vortices in swirl flow. *J. Fluid Mech.* **382**, 195–243.

Bhagwat, M. J. & Leishman, J. G. 2000 Stability analysis of helicopter rotor wakes in axial flight. *J. Am. Helicopter Assoc.* **45**, 165–178.

Boersma, J. & Wood, D. H. 1999 On the self-induced motion of a helical vortex. *J. Fluid Mech.* **384**, 263–280.

Fukumoto, Y. & Okulov, V. L. 2005 The velocity field induced by a helical vortex tube. *Phys. Fluids* **17**, 107101(1–19).

Gupta, B. P. & Loewy, R. G. 1974 Theoretical analysis of the aerodynamic stability of multiple, interdigitated helical vortices. *AIAA J.* **12**, 1381–1387.

Hardin, J. C. 1982 The velocity field induced by a helical vortex filament. *Phys. Fluids* **25**, 1949–1952.

Havelock, T. H. 1931 The stability of motion of rectilinear vortices in ring formation. *Phil. Mag.* **11**, 617–633.

Hopfinger, E. J. & van Heijst, G. J. F. 1993 Vortices in rotating fluids. *Annu. Rev. Fluid Mech.* **25**, 241–289.

Joukowski, N. E. 1912 Vortex theory of a rowing screw. *Trudy Otdeleniya Fizicheskikh Nauk Obshchestva Lubitelei Estestvoznaniya* **16**, (in Russian).

Kuibin, P. A. & Okulov, V. L. 1996 One-dimensional solutions for a flow with a helical symmetry. *Thermophys. Aeromech.* **3**(4), 335–339.

Kurakin, L. G. & Yudovich, V. I. 2002 The stability of stationary rotation of a regular vortex polygon. *Chaos* **12**(3), 574–595.

Landgrebe, A. J. 1972 The wake geometry of a hovering rotor and its influence on rotor performance. *J. Am. Helicopter Soc.* **17**(4), 2–15.

Levy, H. & Forsdyke, A. G. 1928 The steady motion and stability of a helical vortex. *Proc. Roc. Soc. Lond.* A **120**, 670–690.

Margoulis, W. 1922 Propeller theory of Professor Joukowski and his pupils. *NACA Tech. Mem.* 79.

Martemianov, S. & Okulov V. L. 2004 On heat transfer enhancement in swirl pipe flows. *Intl J. Heat Mass Transfer* **47**, 2379–2393.

Medici, D. & Alfredsson, P. H. 2004 Measurements on a wind turbine wake: 3D effects and bluff-body vortex shedding. *Proc. Science of Making Torque from Wind,* 19–21 *April, Delft* (ed. G. A. M. van Kuik), pp. 155-165. DUWIND Deft University of Technology.

Morikawa, G. K. & Swenson, E. V. 1971 Interacting motion of rectilinear geostrophic vortices. *Phys. Fluids* **14**, 1058–1073.

Murakhtina, T. & Okulov, V. L. 2000 Influence of distribution of vorticity in core of swirl flow on the description of spontaneous change in flow regimes. *Thermophys. Aeromech.* **7**(1), 63–68.

Okulov, V. L. 2004 On the stability of multiple helical vortices. *J. Fluid Mech.* **521**, 319–342.

Okulov, V. L. & Fukumoto, Y. 2004 Helical Dipole. *Dokl. Phys.* **49**, 662–667.

Okulov, V. L. & Sorensen, J. N. 2004*a* Instability of the far wake behind a wind turbine. *Abs. 21th ICTAM-2004*, Warsaw, Poland (http://ictam04.ippt.gov.pl/).

Okulov, V. L. & Sorensen, J. N. 2004*b* Instability of a vortex wake behind a wind turbine *Dokl. Phys.* **49**, 772–777.

Ricca, R. L. 1994 The effect of torsion on the motion of a helical filament. *J. Fluid Mech.* **273**, 241–259.

Scully, M. P. 1975 Computation of helicopter rotor wake geometry and its influence on rotor harmonic airloads. *Massachusetts Inst. of Technology Pub.* ARSL TR 178-1.

Vermeer, L. J., Sorensen, J. N. & Crespo, A. 2003 Wind turbine wake Aerodynamics. *Prog. Aerospace Sci.* **39**, 467–510.

Widnall, S. E. 1972 The stability of helical vortex filament. *J. Fluid Mech.* **54**, 641–663.

Wood, D. H. & Boersma, J. 2001 On the motion of multiple helical vortices. *J. Fluid Mech.* **447**, 149–171.